NH_3 condensation in a plate heat exchanger
Experimental investigation on flow patterns, heat transfer and frictional pressure drop

Tao, Xuan; Dahlgren, Elias; Leichsenring, Maaike; Infante Ferreira, Carlos A.

DOI
10.1016/j.ijheatmasstransfer.2020.119374

Publication date
2020

Document Version
Final published version

Published in
International Journal of Heat and Mass Transfer

International Journal of Heat and Mass Transfer 151 (2020) 119374

Contents lists available at ScienceDirect

International Journal of Heat and Mass Transfer

journal homepage: www.elsevier.com/locate/hmt

NH_3 condensation in a plate heat exchanger: Experimental investigation on flow patterns, heat transfer and frictional pressure drop

Xuan Tao*, Elias Dahlgren, Maaike Leichsenring, Carlos A. Infante Ferreira

Process and Energy Laboratory, Delft University of Technology, Leeghwaterstraat 39, 2628 CB, Delft, the Netherlands

ARTICLE INFO

Article history:
Received 16 November 2019
Revised 3 January 2020
Accepted 12 January 2020

Keywords:
Condensation heat transfer
Two-phase frictional pressure drop
Flow patterns
Experimental investigation
Plate heat exchanger
NH_3

ABSTRACT

This paper investigates NH_3 condensation in a plate heat exchanger by visualizing the flow patterns and measuring heat transfer coefficients and frictional pressure drop. Visualization experiments were conducted between 20 and 100 $kgm^{-2}s^{-1}$. Full film flow takes place at large mass fluxes and intermediate mass fluxes of low vapor qualities, while partial film flow occurs at small mass fluxes and intermediate mass fluxes at high vapor qualities. The heat transfer and frictional pressure drop experiments cover the mass fluxes of 21~78 $kgm^{-2}s^{-1}$, the averaged vapor qualities of 0.05~0.65 and the saturated pressure of 630 to 930 kPa. Vapor qualities have significant influences on heat transfer and frictional pressure drop. In the tested ranges, the effect of mass fluxes is noticeable on frictional pressure drop, but is moderate on heat transfer. The impact of saturated pressure is small. The heat transfer reflects the change of flow patterns. The frictional pressure drop shows the characteristics of separated flow.

1. Introduction

In recent decades, the utilization of low grade heat attracts increasing interest given its enormous amount and easy availability. The main resources include solar energy, geothermal energy, the cold energy of LNG, waste heat of industry and seawater (the temperature difference between warm surface seawater and cold deep seawater). The conversion of low grade heat to shaft power can be reached by Organic Rankine Cycles or Kalina Cycles, and is usually implemented in large plants to improve the financial return [1,2,3]. Limited by the small driving temperature difference, large amount of heat needs to be transferred, which requires highly efficient heat exchangers and large charge of working fluid. The heat exchanger effectiveness dominates the overall cycle efficiency.

NH_3 has favorable transport properties and large latent heat. Plate heat exchangers (PHEs) can handle large flow rates and have large heat transfer areas per unit volume. The combination of PHEs and NH_3 is promising for large and intermediate heat loads. The compact structures reduce the charge of working fluid and other equipment investments. PHEs are widely used given their superior heat transfer performance [4,5,6,7].

PHEs mostly have hydraulic diameters of 2~5 mm [8], which are close to the critical diameters of micro or mini channels [9]. The transition from macro-channels to micro-channels happens when surface tension dominates over gravity. It is determined by channel sizes and fluid properties. The large surface tension of NH_3 enhances the micro-channel characteristics during the condensation in PHEs [10]. In the confined channels, the relative magnitudes of surface tension, gravity and shear force differ from those in large smooth tubes. The two-phase interface and wetting characteristics are consequently different. Heat transfer and frictional pressure drop are functions of the occurring flow patterns. NH_3 condensation in PHEs needs to be investigated for what concerns the mechanism of energy and momentum transport.

The flow patterns in PHEs have been experimentally investigated by several researchers. These studies are summarized in Table 1. This paper is focused on two-phase vertical downward flow, which is the common flow direction of condensers and absorbers. Tao et al. [11] presented a detailed overview of previous studies up to 2018. More recently, Buscher [12] carried out visualization experiments on air-water flowing in a PHE horizontally, vertically upward and downward. The flow direction takes effect only at small mass flow rates. During vertical downward flow, big

* Corresponding author.
E-mail addresses: x.tao@tudelft.nl (X. Tao), c.a.infanteferreira@tudelft.nl (C.A. Infante Ferreira).

https://doi.org/10.1016/j.ijheatmasstransfer.2020.119374

Nomenclature

Symbols

A	actual heat transfer area [m^2]
c_p	specific heat capacity [$Jkg^{-1}K^{-1}$]
d_h	hydraulic diameter [mm]
d_p	plate thickness [mm]
g	gravitational constant [ms^{-2}]
G	mass flux [$kgm^{-2}s^{-1}$]
h	enthalpy [Jkg^{-1}]
L_p	port-to-port plate length [mm]
$\dot{m}_a$	mass flow rate [kgs^{-1}]
Nu	Nusselt number [-]
P	pressure [kPa]
Pr	Prandtl number [-]
$\dot{Q}$	heat flow rate [W]
Re	Reynolds number [-]
T	temperature [°C]
U	overall heat transfer coefficient [$Wm^{-2}K^{-1}$]
v	specific volume [m^3kg^{-1}]
x	vapor quality [-]

Greek symbols

α	heat transfer coefficient [$Wm^{-2}K^{-1}$]
β	chevron angle to flow direction [°]
Δ	difference
ρ	density [kgm^{-3}]
λ	thermal conductivity [$Wm^{-1}K^{-1}$]

Subscripts

a	ammonia
$after$	after cooler
av	averaged
de	deceleration
ele	elevation
exp	measured value
fri	frictional pressure drop
G	gas or vapor
in	inlet of test section
L	liquid
mix	mixing process
out	outlet of test section
$port$	ports of test section
sat	at saturated conditions
$test$	test section
$tube$	connected tube
w	water
$wall$	plate wall

bubbles stagnate behind the contact points when the mass flow rates of liquid and vapor are very low. Injection nozzles were specially designed to promote uniform two-phase distribution across the channel width. The homogeneous void fraction model is chosen to predict the transition among bubbly flow, intermittent flow and full film flow. The bubble breakage determines the transition among roundish bubbles, irregular blob-like bubbles and stagnant gas phase. The bubble breakage is modelled according to turbulent kinetic energy. Slug flow and churn flow are not observed. Buscher's [12] flow pattern model excludes phase change and mass transfer. Jiang and Bai [13] visualized air-water flow in a capsule-type PHE, and found that the main flow patterns are film flow, plug flow and churn flow. They proposed transition criteria of the flow patterns. Film flow changes into plug or churn flow when the waves grow large enough to block the gas core. It happens when the liquid flow rate increases and occupies larger flow area. Con-

Table 1
Flow pattern studies for two-phase vertical downward flow in PHEs.

Study	Plate type	Chevron angle	Working fluid	Flow patterns
Tribbe & Müller-Steinhagen [32]	Corrugated	30/30, 30/60, 60/60	Air /Water	Regular bubbly, irregular bubbly, transition between bubbly and churn, churn, film, partial film
Vlasogiannis et al. [33]	Corrugated	60/60	Air /Water	Bubbly, transition between bubbly and rivulet, slug, rivulet
Winkelman [34]	Corrugated	25.7/25.7	Air /Water	Churn, wavy, film, partial film
Nilpueng and Wongwises [31]	Corrugated	35/80	Air /Water	Slug, annular liquid bridge, annular liquid bridge/air alone
Grabenstein and Kabelac [29]	Corrugated	63/63/63/63, 27/27/27/27	Air /Water, R365mfc	Bubbly, slug, film
Grabenstein et al. [30]	Corrugated	63/63/63/63, 27/27/27/27	Air /Water, R365mfc	Bubbly, irregular bubbly, slug, film
Buscher [12]	Corrugated	75/75	Air /Water	Roundish bubble, irregular blob-like bubble, Taylor-like bubble, heterogeneous, partial film, full film, stagnant gas phase
Jiang and Bai [13]	Capsule-type	23.5/66.5[a]	Air /Water	Film, plug, churn

[a] These are the angles between capsules and the vertical direction.

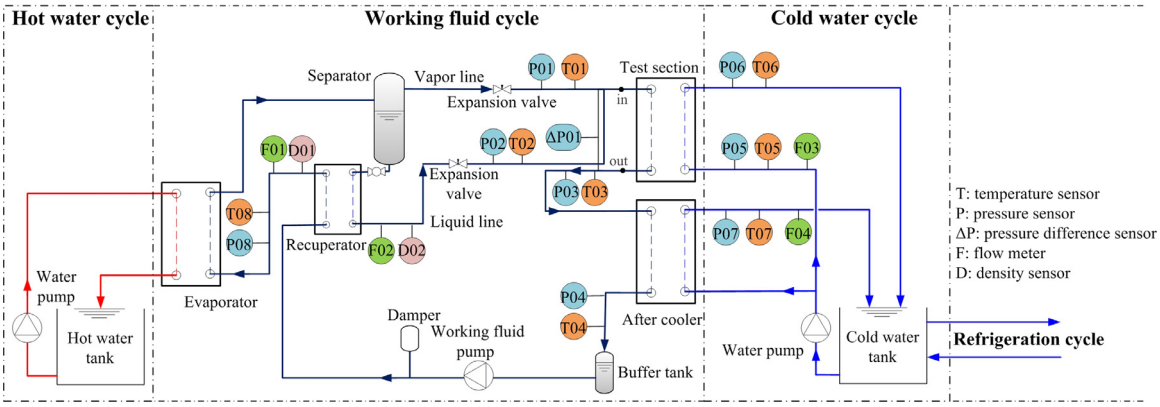

Fig. 1. Diagram of the experimental setup including the working fluid cycle, cold water cycle and hot water cycle.

sequently, the gas pressure decreases. The pressure at the bottom of the waves is larger than at the top, enlarging the waves. Plug flow changes into churn flow when the breaking forces dominate over coalescence forces, which are determined by turbulence and surface tension, respectively.

In general, the visualization experiments of PHEs mostly used air-water and were without phase change. The flow patterns of condensing NH_3 are different because of the distinct two-phase density ratio and surface tension in comparison to air-water. Additionally, the vapor qualities decrease from the inlet to the outlet during diabatic flow, gradually changing the flow patterns.

Despite the promising performance of PHEs in NH_3 systems, the research on condensation is limited. The condensation of HFCs, hydrocarbons and HFOs in PHEs has been widely investigated by experiments, but reports on NH_3 data are scarce [8]. NH_3 is characterized by large thermal conductivity, surface tension and latent heat. The heat transfer and frictional pressure drop correlations derived from HFCs or hydrocarbons are hardly applicable for NH_3. The deviations depend on the channel sizes. These correlations over-predict the experimental heat transfer coefficients (HTCs) of a large diameter tube (8 mm), but under-predict the HTCs of small diameter tubes (0.98, 1.44 and 2.16 mm) [14,15,16].

This paper investigates NH_3 condensation in PHEs and presents the experimental data of two-phase flow resulting from the distinct fluid properties of NH_3. Sections 2 and 3 describe the experimental setup and methods. Section 4 discusses the flow patterns including full film flow and partial film flow. In Section 5, the experimental results of heat transfer and frictional pressure drop are analysed based on flow patterns. The flow patterns give insight into the characteristics of separated flow and reveal the physical processes during NH_3 condensation in PHEs, and in this way form the basis to develop mechanistic models of HTCs and frictional pressure drop.

2. Experimental setup

The experimental setup was originally built as an ocean thermal energy conversion system, and can operate as Organic Rankine Cycle or Kalina Cycle with NH_3 and NH_3/H_2O, respectively. The setup is composed of a working fluid cycle, a hot water cycle and a cold water cycle.

2.1. Working fluid and water cycles

Fig. 1 shows the process flow diagram. NH_3 is heated by hot water in an evaporator, where it is partially evaporated. The two phases flow into a separator, after which the vapor flows through an expansion valve with the pressure being reduced. The liquid is subcooled in a recuperator and flows through an expansion valve. The two phases are controlled to be at the same pressure and mix up before entering the test section. The fluid is partially condensed in the test section by the cold water, and then is subcooled in an after cooler. Afterwards, it flows into a buffer tank. The liquid level in the buffer tank decreases for large mass flow rate, providing the upper limit of the mass flow rate. A variable speed diaphragm pump controls the flow rate of the NH_3. Diaphragm pumps are suitable for corrosive fluids like NH_3, and are able to cope with cavitation. In order to reduce the fluctuation of flow rate and operating pressure, a damper filled with nitrogen is installed at the outlet of the working fluid pump. The mass flow rate becomes unstable for small values, limiting the lowest mass flow rate. Next, NH_3 flows through the recuperator into the evaporator.

Three brazed plate heat exchangers act as the evaporator, recuperator and after cooler. A sight glass is inserted into the separator to observe the liquid level. Two relieve valves are installed after the pump and before the separator. These valves open when the absolute pressure is above 1600 kPa. The setup is wrapped with a layer of insulation material of 20 mm, while the test section is insulated with two layers.

The cold water cycle feeds both the test section and after cooler in parallel. The cold water is pumped and separated to these two heat exchangers. The water pump is a centrifugal pump. The inlets of the test section and after cooler have the same temperature and pressure, and share sensors. The flow rates of both lines are measured to determine the heat transfer rate. Water is mixed in a tank. The flow rate and temperature at the heat exchanger inlet are controlled by the water pump and a refrigeration cycle. During the experiments, the water side mass flow rate was close to the maximum attainable value by the pump to increase this HTC. A PID temperature controller is implemented to achieve the desired water temperature. The cold water cycle has a cooling capacity of about 6000 W at 8 °C.

The hot water cycle is composed of a tank, an electrical heater, a centrifugal pump and sensors. The heat transfer rate to the evaporator is determined by the water flow rate and temperature glide. The flow rate and temperature at the evaporator inlet are controlled by the water pump and heater. The heater has a maximum capacity of 6000 W.

2.2. Measurement instrumentation

Temperature and pressure are measured at several positions of the set up. For simplicity, Fig. 1 only shows the sensors that are relevant for the discussion of this paper. The temperature and pres-

Table 2
Specification of the sensors.

Sensors	Type	Sensor uncertainty	Range
Temperature	PT-100	±0.05 °C	2 /50 °C
NH_3 pressure	Absolute	±0.05% FS	0/1000 kPa
NH_3 pressure	Gauge	±0.5% FS	0/1000 kPa
Water pressure	Gauge	±0.5% FS	0/250 kPa
Differential pressure	SITRANS P DS	±0.3% FS	1.6 /160 kPa
NH_3 overall flow	Coriolis	±0.2% RD	0 /0.02 kgs^{-1}
NH_3 liquid flow	Coriolis	±0.2% RD	0 /0.013 kgs^{-1}
Water	Turbine	±1% FS	30
flow		±7.2 Lh^{-1} [a]	/3000
NH_3 density	Anton Paar	±0.1 kgm^{-3}	Lh^{-1}

[a] These sensors have an uncertainty of ±1% FS in the full range. The measured value of F03 is kept almost constant at 432 Lh^{-1} during experiment. F03 is calibrated in this range with an uncertainty of ± 7.2 Lh^{-1}.

sure of NH_3 are measured at the following positions: the vapor and liquid inlets of the test section, as well as the outlets of the test section and after cooler. The NH_3 pressure drop within the test section is also measured. The overall and liquid mass flow rates of the working fluid are measured at the inlet of the evaporator and at the liquid line. The ratio of mass flow rates is used to check the vapor quality at the test section inlet. The temperature and pressure of the cold water are measured at the inlet and outlet of the test section and after cooler, as well as its volume flow rate. Density is measured by D01 at the same location as the overall NH_3 mass flow rate. When the setup is operated with NH_3/H_2O, the density is used to determine the bulk NH_3 concentration.

Table 2 lists the sensor features. The measurement system was originally described by Tao et al. [17], and was further modified to improve the accuracy and to extend the measurement range. Temperature is measured with four-wire PT-100 of high precision. The uncertainty is ±0.05 °C in the operating ranges. NH_3 pressure is measured by two types of sensors. P03 and P08 are absolute pressure sensors, and the uncertainty is ±0.05% FS. The other NH_3 pressure sensors are gage pressure sensors and have an uncertainty of ±0.5% FS. The water pressure sensors are also gage pressure sensors with ±0.5% FS uncertainty. The pressure drop of NH_3 within the test section is measured by a differential pressure sensor of ± 0.3% FS uncertainty. The NH_3 mass flow rate is measured by Coriolis type mass flow meters of ±0.2% RD uncertainty. The water flow meters originally have an uncertainty of ±1% FS and considerably contribute to the uncertainty of condensation HTCs. The water flow rate was kept at the maximum value available by the pump and was almost constant. F03 is specially calibrated in the tested range and has an uncertainty of ±7.2 Lh^{-1}. The uncertainty of the NH_3 density sensor is ±0.1 kgm^{-3}.

Data are acquired and recorded with LabVIEW. It also implements control and safety protection. A program is developed to analyze the measured data. In order to determine the steady state, the time derivatives of all the measured data are calculated. Both the slopes and amplitudes are assessed. Pressure and mass flow rate fluctuate mostly after the working fluid pump, and are stabilized by adjusting the damper. The steady state is kept for more than 10 min, and the time averaged values are used for data reduction.

2.3. Test section: gasketed plate heat exchanger and transparent plate

The test section is a gasketed plate heat exchanger (GPHE) with the plate number adjustable. In order to avoid the flow maldistribution among channels, the GPHE consists of three plates forming two channels during the experiments. Only one plate is effective for heat transfer. NH_3 flows vertically downward in one channel, while cold water flows upward in the other channel. These three plates are pressed by frame plates from both sides. Fig. 3 illustrates the plate of the GPHE, and Table 3 gives the geometrical parameters. Tao et al. [11] define these parameters. The GPHE is assembled from Alloy 316 plates and EPDM gaskets to be compatible with NH_3.

The plate has triangular inlet and outlet areas, where flow is distributed from the inlet port or into the outlet port. The plate surface is composed of sinusoidal corrugations, where the grooves can be considered as branching sub-channels in parallel. The grooves on one plate have an opposite direction with those on the adjacent plate. Fluid flows along the grooves, which is similar to inclined downward flow. Meanwhile, the fluid also passes across the grooves at the contact points of adjacent plates.

As shown in Fig. 2, a transparent plate is fabricated to visualize the condensing flow. This plate has the same geometry as the metal plates except that the plate thickness is 25 mm. The corrugated surface is replicated so that the flow patterns during condensation are able to reappear. The visualization test section is composed of two metal plates and the transparent plate. The frame plate adjacent to the transparent plate has three observation windows. The visualization experiment is diabatic. The flow directions of NH_3 and cold water are the same as during the heat transfer experiments.

The transparent material is required to be machinable and compatible with NH_3. Tao et al. [11] summarized the transparent materials used to manufacture PHEs applicable for air-water, which are not compatible with NH_3. Kim et al. [18] and Nakamura et al. [19] 3D printed transparent plates of small sizes. Lee et al. [20] fabricated a transparent plate with polycarbonate. da Silva Lima et al. [21] and Arima et al. [22] used sight glass to fabricate smooth tubes and smooth plates for NH_3 visualization, but sight glass is not machinable. In order to test the compatibility, the samples of several polymers were immersed into liquid NH_3. Polystyrene (PS) has better compatibility compared with polymethylmethacrylaat (PMMA), polyvinylchloride (PVC), polycarbonate (PC) and terephthalate glycol (PETG). But PS may decay after long time operation. Leichsenring [23] and Leichsenring et al. [24] presented the details of material selection and strength analysis. The transparent plate is manufactured by glueing a layer of PS and a layer of PMMA. The PS plate contacts NH_3, which has a thickness of 5 mm and was machined. The PMMA plate improves the mechanical strength. It is 20 mm thick and is pressed by the frame plate. The visualization experiment lasted for 2 weeks. After then, the transparent plate started to decay so the experiment had to be stopped.

Flow patterns were captured with a high speed camera from the front, with a frame rate of 3000 fps and a resolution of 1024×1024 pixels. The transparent plate was wrapped with an LED-strip on the sides circumferentially. The channel is well illuminated as shown in Fig. 2 (Right).

Table 3
Geometrical parameters of the test section.

Plate number	Port-to-port plate length	In gasket plate width	Heat transfer area	Hydraulic diameter	Chevron angle	Enlargement factor	Channel gap	Plate thickness	Corrugation wavelength
–	mm	mm	m^2	mm		–	mm	mm	mm
3	668	95	0.640	2.99	63°	1.15	1.72	0.58	6.67

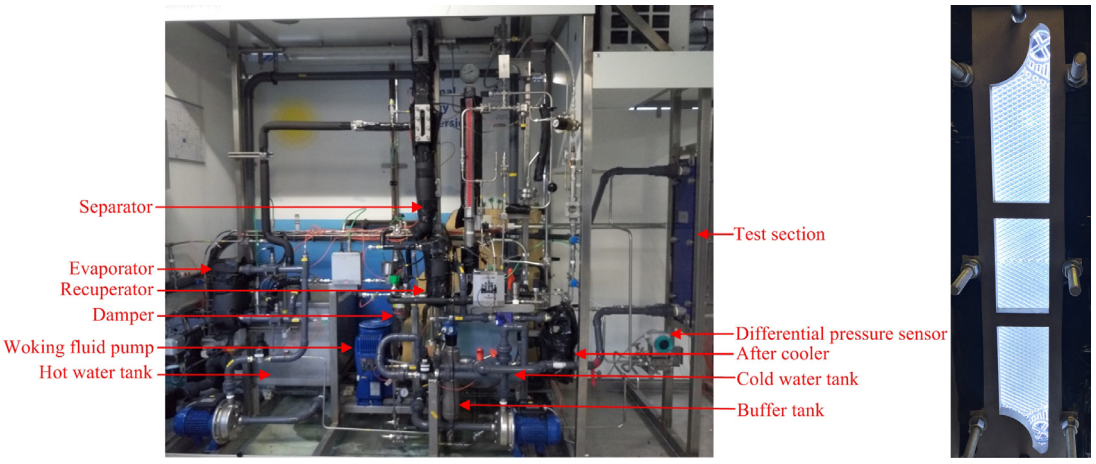

Fig. 2. Pictures of the experimental setup and visualization section.

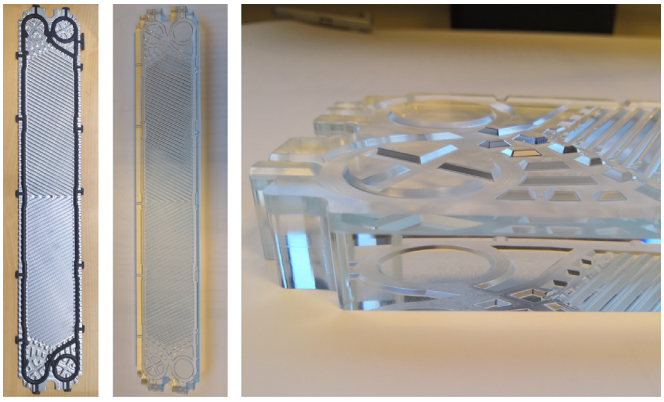

Fig. 3. Pictures of the stainless steel plate and transparent plate.

3. Data reduction

In Eqs. (1) and (2), the inlet and outlet NH_3 enthalpies of the test section, $h_{a,\,in}$ and $h_{a,\,out}$, are determined from the energy balance of the after cooler and test section. The inlet and outlet vapor qualities are determined referring to Refprop 9.1 [25]. The averaged vapor quality is used to analyze the flow patterns, heat transfer and frictional pressure drop data. The inlet and outlet vapor qualities are also used to illustrate the flow patterns. The condensation HTC, α_a, is calculated using Eq. (3). The condensation temperature, T_a, changes slightly from the inlet to the outlet because of the frictional pressure drop. The water HTC, α_w, is presented in Eq. (4) [26]. It has been derived from H_2O–H_2O experiments using Wilson-plot method.

$$h_{a,out} = h_{a,04} + \frac{\dot{Q}_{after}}{\dot{m}_{a,01}} = h_{a,04} + \frac{c_{p,w}\dot{m}_{w,04}(T_{w,07} - T_{w,05})}{\dot{m}_{a,01}} \tag{1}$$

$$h_{a,in} = h_{a,out} + \frac{\dot{Q}_{test}}{\dot{m}_{a,01}} = h_{a,out} + \frac{c_{p,w}\dot{m}_{w,03}(T_{w,06} - T_{w,05})}{\dot{m}_{a,01}} \tag{2}$$

$$\begin{aligned}\dot{Q}_{test} &= \dot{m}_{w,03}c_{p,w}(T_{w,06} - T_{w,05}) = \dot{m}_{a,01}\left(h_{a,i_n} - h_{a,out}\right)\\ &= UA\frac{(T_{a,in} - T_{w,06}) - (T_{a,out} - T_{w,05})}{\ln\frac{T_{a,in} - T_{w,06}}{T_{a,out} - T_{w,05}}}\\ &= \frac{A}{\frac{1}{\alpha_a} + \frac{d_p}{\lambda_{wall}} + \frac{1}{\alpha_w}}\frac{(T_{a,in} - T_{w,06}) - (T_{a,out} - T_{w,05})}{\ln\frac{T_{a,in} - T_{w,06}}{T_{a,out} - T_{w,05}}}\end{aligned} \tag{3}$$

$$Nu_w = \frac{\alpha_w d_h}{\lambda_w} = 0.275 Re_w^{0.7} Pr_w^{1/3} \qquad 320 \le Re_w \le 2600 \tag{4}$$

Eq. (5) calculates the frictional pressure drop of condensation, $\Delta P_{fri,a}$, by subtracting the other components from the measured pressure drop, $\Delta P_{\exp,\,a}$. In Eqs. (6) and (7), the pressure drops of inlet and outlet ports, $\Delta P_{inport,\,a}$ and $\Delta P_{outport,\,a}$, are treated as sudden enlargement and sudden contraction of two-phase flow [27]. In Eqs. (8) and (9), the deceleration pressure rise, $\Delta P_{de,\,a}$, and elevation pressure rise, $\Delta P_{ele,\,a}$, use the homogeneous two-phase model [27]. The mixing pressure drop, $\Delta P_{mix,\,a}$, regards the spraying of liquid into vapor through orifices, and is calculated according to Jankowski et al. [28]. The details of the calculation are specified in Tao et al. [26]. The frictional pressure drop of condensation accounts for more than 90% of the measured pressure drop.

$$\begin{aligned}\Delta P_{fri,a} = {} & \Delta P_{\exp,a} - \Delta P_{inport,a} - \Delta P_{outport,a} - \Delta P_{mix,a}\\ & + \Delta P_{de,a} + \Delta P_{ele,a}\end{aligned} \tag{5}$$

$$\Delta P_{in\ port,a} = G_{tube}^2 v_L \frac{A_{tube}}{A_{port}}\left(1 - \frac{A_{tube}}{A_{port}}\right)\left(1 + \frac{v_G - v_L}{v_L}x\right) \tag{6}$$

$$\Delta P_{out\ port,a} = \frac{G_{tube}^2 v_L}{2}\left(\frac{1}{0.591} - 1\right)^2\left(1 + \frac{v_G - v_L}{v_L}x\right) \tag{7}$$

$$\Delta P_{de,a} = G^2(v_G - v_L)(x_{in} - x_{out}) \tag{8}$$

$$\Delta P_{ele,a} = \rho_{av} g L_p \tag{9}$$

4. Flow visualization results

Visualization experiments of NH_3 were conducted at the condensation pressure of 690 kPa. The flow patterns changed with vapor qualities and mass fluxes. Only film flow has been detected. Air-water experiments observed bubbly flow, slug flow, churn flow, film flow or the equivalent flow patterns [12,29,30,31,32,33,34]. Bubbly flow is known to be limited at large mass fluxes and low vapor qualities. The kinetic energy is strong enough to break up the bubbles, and the bubble breakup overcomes coalescence. The condensing NH_3 in the present paper was below 100 $kgm^{-2}s^{-1}$. By contrast, bubbly flow of air and water happens above the overall mass flux of approximately 100 $kgm^{-2}s^{-1}$ [12,29,30,32,33]. Buscher [12] did not observe slug flow or churn flow, which is characterized by the phenomenon that the whole channel width is occupied by gas or liquid periodically. In tubes, bubbles move faster

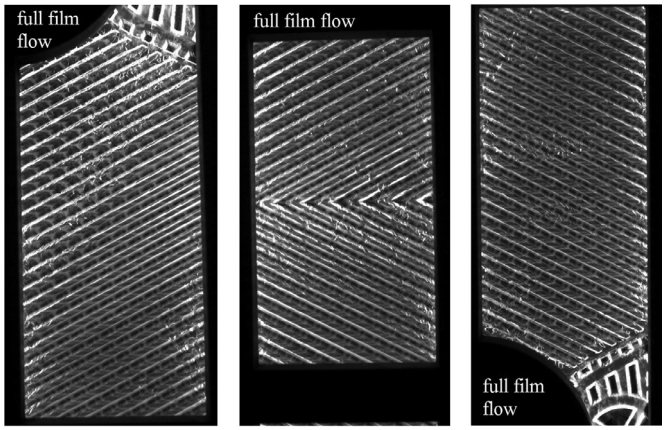

Fig. 4. Full film flow with $G = 81$ kgm^{-2}s^{-1} and x_{av}= 0.30 at the top, middle and bottom windows. The corresponding videos are included in the Supplementary materials of the online version.

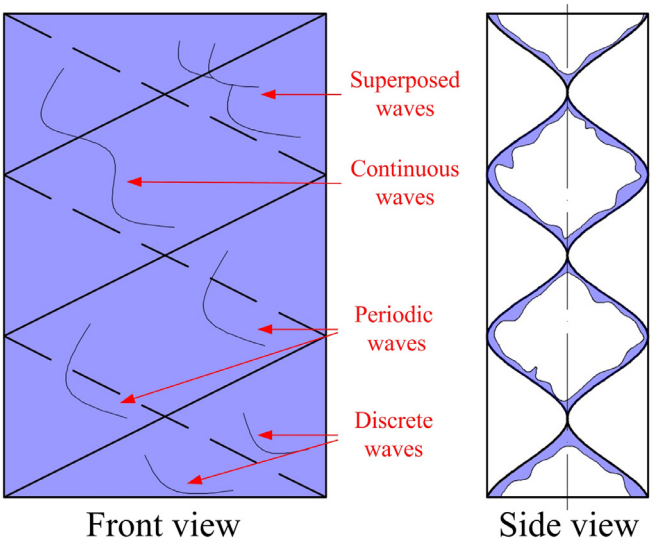

Fig. 5. Schematic of full film flow. Indicating different kinds of waves.

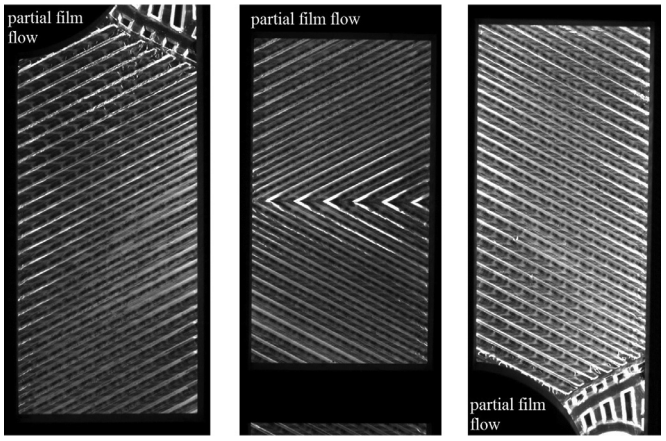

Fig. 6. Partial film flow with $G = 43$ kgm^{-2}s^{-1} and x_{av}=0.46 at the top, middle and bottom windows. The corresponding videos are included in the Supplementary materials of the online version.

with growing sizes, and coalesce more intensively. However, in the corrugated channels, the centrifugal forces weaken bubble acceleration and suppress two-phase separation. The slug or churn flow in other researches is mainly attributed to the gas-liquid injection [12].

The test section could not be insulated from the front, which results in some heat leak. According to uncertainty analysis, the heat leak has minor influences on vapor quality, but brings about significant errors to HTCs. Thus the condensation HTCs cannot be derived. The outlet vapor qualities are determined from the energy balance of the after cooler, and are not influenced by the heat leak. The inlet vapor qualities are based on the energy balance of the test section, and are affected by the heat leak. The effect is small since NH_3 has large latent heat. This has been checked making use of the overall and liquid flow meters.

4.1. Flow patterns

The terms film flow and partial film flow are used in previous papers. In order to clarify the wetting characteristics, in this paper, *full film flow* describes the flow pattern for which the wall is completely wetted, while *partial film flow* indicates part of the wall is dry. *Film flow* is the sum of full film flow and partial film flow.

Fig. 4 shows the pictures of full film flow, which is similar to annular flow in tubes. The videos of full film flow are provided in the Supplementary materials of the online version of this paper. Fig. 5 illustrates the distribution of liquid and vapor. Continuous liquid film flows on the wall, while vapor core flows in the center of the groove. Because of the corrugated groove, the two-phase interface is rough even at low mass fluxes. Waves and ripples move at the interface. The waves are dispersed with varying wavelengths and amplitudes, and grow larger with increasing mass fluxes. Various flow phenomena are observed, and are shown in Fig. 5. For superposed waves, several waves interact with each other, making the flow more chaotic. Continuous waves have connected waves that flow at the same speed. These waves extend over adjacent grooves. Periodic waves flow in the same paths and have almost the same shapes. The rest waves are discrete and are independent of the other waves.

The waves gradually decrease in amplitude from the inlet to the outlet. In the inlet region, the liquid and vapor are distributed into adjacent grooves, and pass across grooves intensively. Additionally, the vapor quality decreases along the flow direction, which reduces the kinetic energy gradually. The vapor phase has larger velocity than the liquid phase, and tears liquid droplets off the film. The channel of the PHE is so narrow that droplets are easily deposited on the other side of the wall. Consequently, no stable entrained liquid droplets are formed in the vapor core.

Fig. 6 shows partial film flow. It occurs when the liquid mass flux is reduced. Less liquid is attributed to higher vapor quality or smaller mass flux. The liquid is not enough to wet the entire wall, and parts of the wall become dry. NH_3 has large surface tension, whose influence becomes prominent in small diameter channels. Large contact angles reduce the wetting ability, break up the liquid film and change the flow pattern [35]. Large surface tension makes the liquid film discontinuous [36]. Additionally, surface tension tends to stabilize the flow and suppress the waves [37]. The videos of partial film flow are provided in the Supplementary materials of the online version.

As shown in Fig. 7, two types of dry zones coexist. In the first type, whole pieces of zones become dry, and the areas of these zones increase with decreasing liquid mass fluxes. In the inlet region next to the port, liquid and vapor are distributed into the parallel grooves. When the areas of these zones are small, dry zones are located close to one edge of the plate, and have triangular shapes. When these areas increase, the dry zones grow until covering most part of the plate. In the second type, dry spots are discretely distributed in the corrugated grooves. Under gravity force, these dry zones tend to appear at the top of the grooves.

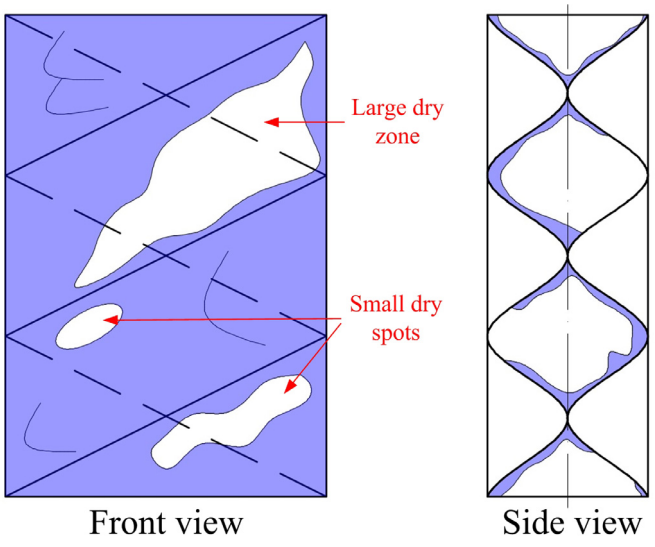

Fig. 7. Schematic of partial film flow. Indicating different types of dry zones.

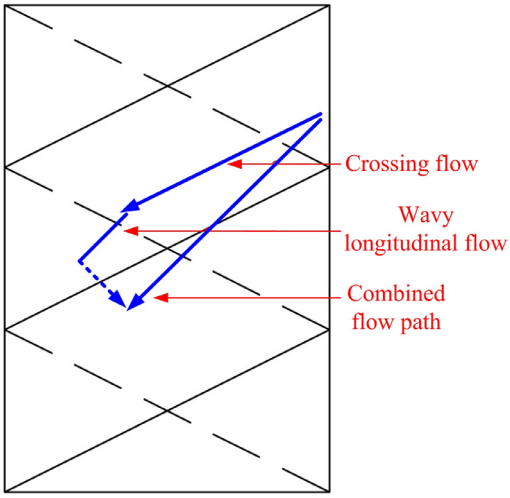

Fig. 8. Schematic of liquid flow paths. The observed flow path is a combination of crossing flow and wavy longitudinal flow.

This flow is similar to stratified flow in inclined downward tubes. The properties of the wall surface affect the fluid motion, and the flow direction of the fluid changes when the surface is inhomogeneous [38]. The temperature distribution of the corrugated surface is slightly inhomogeneous because the cold water crosses the contact points and forms vortices in the grooves within the adjacent channel [39]. The variation of wall temperature makes the liquid distribute unevenly. In both types, vapor condenses directly at the wall. These zones seem to be covered with a thin condensate layer, which makes it different from adiabatic flow. The layer is so thin that the observation can be subjective and needs further discussion. Vapor condensates on the wall as long as the wall temperature is below the saturated temperature [40,41]. During the present experiments, the inlet of the working fluid is in the two-phase region and is not superheated. The averaged wall temperature is lower than the saturated temperature for more than 1 K. Theoretically, condensation takes place once the vapor is in contact with the wall. Moreover, the occurrence of condensation can be proved from the opposite perspective. The dry zones become ineffective if condensation does not take place, and the heat transfer deteriorates because the effective area is reduced. However, the heat transfer is enhanced for partial film flow. This will be further discussed in Section 5.1.

The waves for partial film flow are weaker than for full film flow because of the smaller liquid mass flux. The liquid film of partial film flow is relatively thin. Thin film tends to be laminar, and the structure of two-phase interface is smoother. Deposition of entrained liquid droplets has been observed at the dry zones.

4.2. Flow paths and flow distribution

Flow paths were originally used to describe the flow direction of single phase flow [[42,39]. During two-phase flow, the liquid phase is traced by the movement of waves. Fig. 8 schematically shows the flow paths of the liquid phase. Crossing flow goes from one side of the plate to the other side, and reflects at the edge of the plate, changing direction. Waves are more intensive close to the edge. Wavy longitudinal flow circles the contact points of two adjacent plates. The observed flow is a combination of both paths, and crossing flow is dominant. The liquid flows along grooves, and gradually goes across the grooves. The direction shifts downward. The combined flow paths make the flow turbulent at small mass fluxes, so PHEs have larger HTCs and frictional pressure drop than tubes.

Buscher [12] and Tribbe and Müller-Steinhagen [32] traced the flow paths of bubbles during bubbly flow. Crossing flow is dominant with small chevron angles (30°), while wavy longitudinal flow prevails with large chevron angles (60° and 75°). The chevron angle of the plates used in this study is 63°, and crossing flow dominates during film flow. It is expected to be wavy longitudinal flow if bubbly flow occurs. The difference between homogeneous flow and separated flow plays a role. Bubbly flow is considered as homogeneous flow, and is similar to single phase flow. Film flow is separated flow, and shows distinct characteristics.

The maldistribution of liquid and vapor is more severe close to the inlet port. The liquid phase has larger momentum than vapor, and the flow splits among the grooves. Liquid preferentially flows into the front grooves directly connected to the inlet port, while vapor is distributed into all the grooves. The flow distribution becomes uniform in the downward direction. The flow reflects and recirculates at the edge, which improves the two-phase distribution. In the downward direction, the wave amplitudes decrease and the two-phase interface becomes smoother. Similar distribution was observed during the visualization of air-water flow without phase change [34].

4.3. Flow pattern map

Fig. 9 presents the flow pattern map plotted with the mass flux and vapor quality, which indicates the condensation process. The map includes the flow patterns at the inlet, middle and outlet of the test section, which were observed from the three windows. The data points are assigned to the inlet, averaged and outlet vapor qualities, respectively. These three flow patterns for each operating condition are connected by lines. The condensation is from the right end to the left end of the lines. The change of vapor qualities is small. At large and small mass fluxes, the flow patterns remain the same from the inlet to outlet, while the flow patterns change in the flow direction for intermediate mass fluxes.

Full film flow occurs at large mass fluxes or the combination of intermediate mass fluxes and low vapor qualities. On the contrary, partial film flow is at small mass fluxes or the combination of intermediate mass fluxes and high vapor qualities. Flow patterns depend on the liquid mass flux. A certain amount of liquid is required to completely wet the wall surfaces, otherwise the thin liquid film breaks up. The minimum wetting mass flux depends on

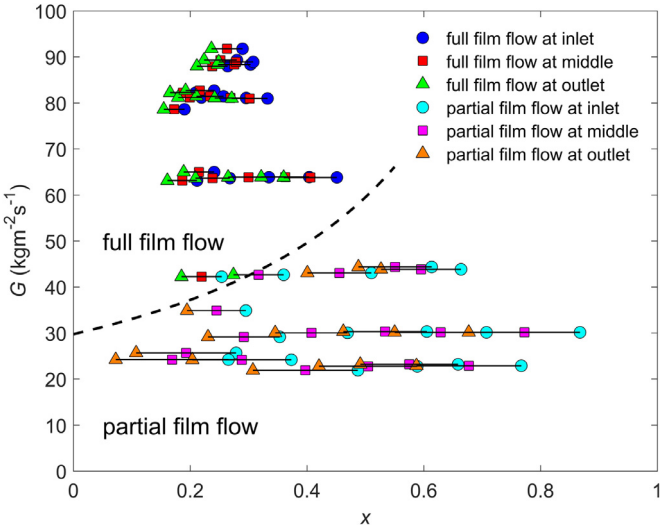

Fig. 9. Flow pattern map of condensing flow in the PHE, with the vapor quality decreasing from the inlet to the outlet. The flow patterns at the inlet, middle and outlet windows of the same operating condition are connected by lines.

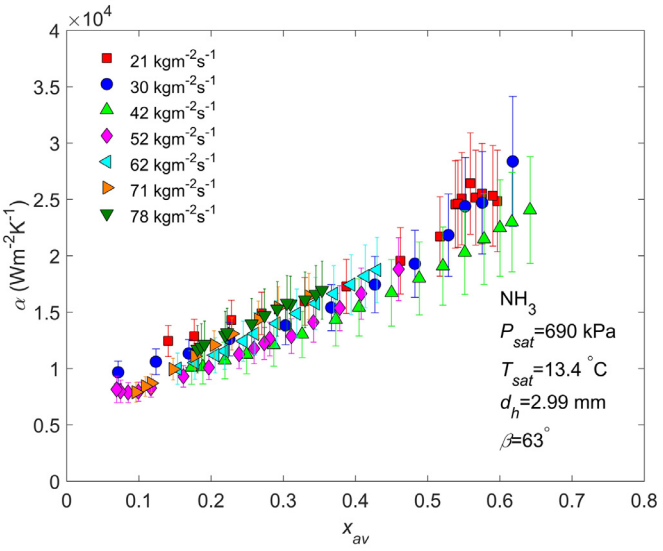

Fig. 10. Condensation HTCs with varying averaged vapor quality at different mass fluxes.

the surface tension, liquid density and liquid viscosity. The liquid velocity distribution is not uniform especially for large contact angles [43,44]. At intermediate mass fluxes of low vapor qualities, partial film flow changes into full film flow from the inlet to the outlet. These data points are considered to be in the transition region. The vapor quality decreases in the flow direction with increasing liquid mass fluxes. Moreover, the flow distribution among grooves becomes more uniform after reflection at the plate edges. This phenomenon illustrates the influence of the inlet distributing region on flow patterns. Partial film flow occurs at small mass fluxes. In the top window, dry zones are continuous and stretch. In the middle and bottom windows, liquid tends to be distributed among grooves uniformly. Dry spots are discrete in each groove.

5. Experimental data and discussion

Condensation experiments of NH_3 are carried out. The sensitivity of HTCs and frictional pressure drop to vapor qualities, mass fluxes and saturated pressures is investigated. Because of the large latent heat, the change of the vapor qualities is small, and the following discussion is represented with the averaged vapor qualities. The measured HTCs and frictional pressure drop are considered to be quasi-local. During the experiments, some data points were repeated by increasing and decreasing the heating capacity, respectively. The repeatability is proved to be reliable.

5.1. Heat transfer coefficient

The condensation HTCs are large, and the corresponding heat transfer resistances are relatively small compared with the water side. In order to improve the measurement accuracy, the water side mass fluxes were kept large to reduce the corresponding heat transfer resistance. In the tested ranges, the ratio of heat transfer resistance between the condensation side to water side has an averaged value of 1.6. Additionally, the accurate measurement of the heat duty requires large rise of the cold water temperature, whose averaged value is 2.8 K during testing. HTCs larger than 30,000 $Wm^{-2}K^{-1}$ are excluded because of their large uncertainty.

Fig. 10 illustrates the HTCs variation with averaged vapor qualities and mass fluxes. The saturated pressure is 690 kPa. It covers the averaged vapor qualities of 0.05~0.65 and mass fluxes of 21~78 $kgm^{-2}s^{-1}$. Limited by the cooling capacity of the setup, higher vapor quality cannot be obtained. HTCs increase sharply and almost linearly with vapor qualities. For 42 $kgm^{-2}s^{-1}$, the HTCs increase 2.5 times when the averaged vapor qualities rise from 0.2 to 0.65. A slight rise of the vapor quality increases the volume flux noticeably. The transition of flow patterns has been observed during the visualization experiments. With increasing vapor qualities, the vapor velocity increases and the film thickness decreases. Larger shear force disturbs the two-phase interface and enhances the heat transfer. Moreover, at high vapor qualities, the liquid film is locally extremely thin. The vapor condenses directly on the wall and the heat transfer resistance is small. Since NH_3 has a large two-phase density ratio, the sensitivity to vapor quality is stronger than for other refrigerants such as R134a and R410A [45].

The influence of mass fluxes is not monotonic. HTCs decrease slightly with mass fluxes in the range of 21~42 $kgm^{-2}s^{-1}$, and increase moderately from 42 to 78 $kgm^{-2}s^{-1}$. It is attributed to the change of flow patterns. At small mass fluxes, a part of the wall surface is dry due to small amounts of liquid. The vapor velocity is low, and only limited shear force is exerted on the two-phase interface. Thus the liquid film is laminar. The condensation process is divided into two parts. Some vapor condenses directly on the wall, while other condenses on the two-phase interface where the wall is wetted. Gravity-controlled condensation dominates over convective condensation. For a certain vapor quality, the portion of wetted surface increases with mass fluxes because of more liquid. Consequently, the heat transfer resistance slightly increases. At large mass fluxes, the wall surface is completely wetted. Shear force is dominant, and convective condensation applies. For a certain vapor quality, the mass fluxes of both vapor and liquid increase. Higher vapor velocities intensify shear force and promote ripples on the two-phase interface. On the one hand, the liquid film becomes turbulent with increasing mass fluxes. But on the other hand, thicker liquid film increases the heat transfer resistance. As a consequence, HTCs increase moderately with mass fluxes at large values. In Fig. 10, the averaged uncertainty of HTCs is ±14.4%. The measurement uncertainty is contributed by temperature sensors and flow meters. The temperature difference is smaller for higher HTCs, and the relative error becomes significant, which contributes prominently to the uncertainty propagation.

In Fig. 11, the influence of saturated pressure is shown at two mass fluxes. The trends at these mass fluxes are similar, and only the values at 52 $kgm^{-2}s^{-1}$ are discussed. HTCs decrease slightly

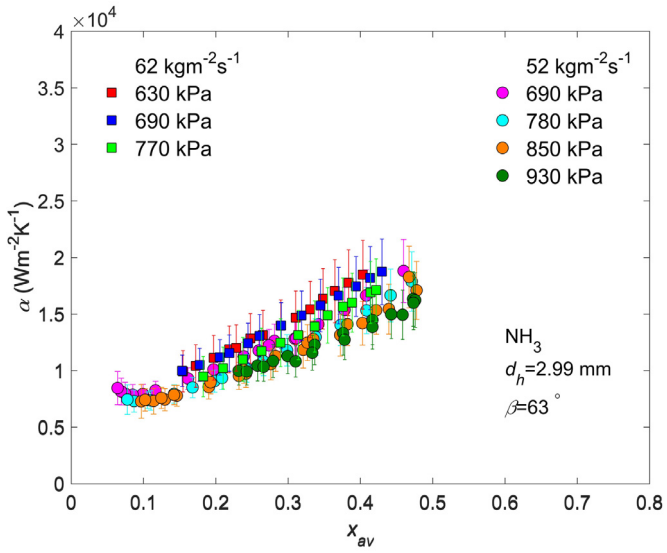

Fig. 11. Condensation HTCs with varying averaged vapor quality at different condensation pressures.

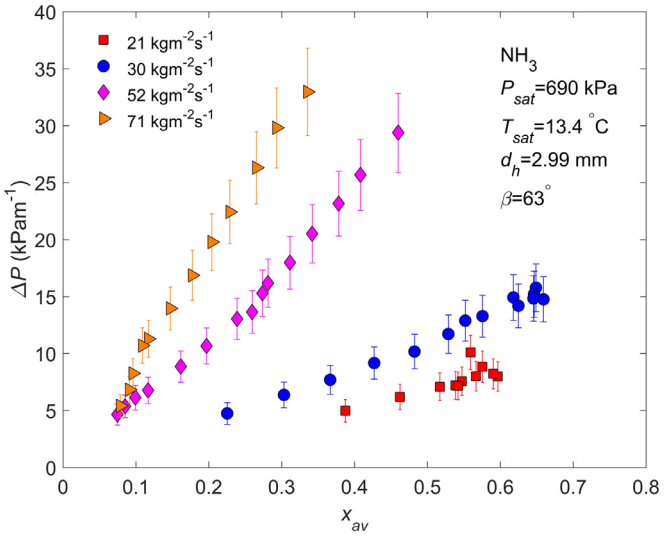

Fig. 13. Frictional pressure drop with varying averaged vapor quality at different mass fluxes.

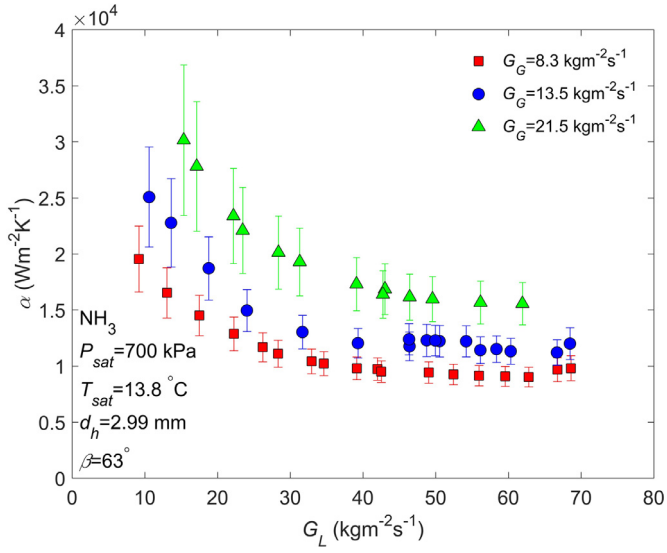

Fig. 12. Condensation HTCs with varying liquid and vapor mass fluxes.

with increasing saturated pressure, and become about 20% lower from 690 to 930 kPa. Higher saturated pressure has smaller two-phase density ratio, and the shear force at the interface is reduced. The thermal conductivity of liquid also decreases at higher pressure. Despite the minor effect of saturated pressure, the influence of vapor qualities is still significant. The averaged uncertainty of HTCs is ±14.1% according to the uncertainty analysis.

Fig. 12 further presents the influence of liquid and vapor mass fluxes. The visualization experiments have indicated separated flow. For this reason the two-phase mass fluxes are investigated separately.

The slope of HTCs for a certain vapor mass flux is divided into two parts. HTCs decrease noticeably with increasing liquid mass fluxes at small values, and stay almost constant at larger values. The liquid film is the main heat transfer resistance during condensation. At small liquid mass fluxes, partial film flow applies, and a part of the wall surface is not wetted. Vapor condensates directly on the wall. The area of the dry zones decreases with increasing amount of liquid, and the HTC decreases significantly. At a certain value, the wall gets completely wetted. It becomes full film flow. Further increase of mass flux thickens the liquid film. Meanwhile, the liquid flow becomes more turbulent. These two effects counteract each other. Consequently, HTCs remain constant. The slope of HTCs changes at the liquid mass fluxes of around 40 $kgm^{-2}s^{-1}$. Partial film flow has larger HTCs than full film flow. This confirms that condensation takes place in the dry zones and indicates that all the heat transfer area is effective during partial film flow.

Larger vapor mass fluxes enhance the heat transfer. Higher vapor velocities intensify the two-phase shear and thin the liquid film. The enhancement is larger for partial film flow. Droplet entrainment is promoted by the higher vapor velocities and tends to increase the heat transfer.

5.2. Frictional pressure drop

Fig. 13 shows the influence of averaged vapor qualities and mass fluxes on frictional pressure drop. At certain mass fluxes, frictional pressure drop increases almost linearly with vapor qualities. The increase is sharper at large mass fluxes. When the averaged vapor qualities have an increment of 0.1, the frictional pressure drop increases about 10 $kPam^{-1}$ for 71 $kgm^{-2}s^{-1}$ and increases 2 $kPam^{-1}$ for 30 $kgm^{-2}s^{-1}$. The flow patterns have relatively small influences on frictional pressure drop compared with heat transfer [20]. Both full film flow and partial film flow are separated flows. Liquid and vapor flow separately and interact on the interface. The two-phase pressure drop is contributed by the following shear forces: between the vapor and wall, between the liquid and wall and at the two-phase interface. The volume flux and averaged velocity increase significantly with vapor quality, and the shear forces are greatly enhanced.

Frictional pressure drop increases sharply with mass fluxes. Larger liquid mass flux thickens the film thickness and promotes turbulence. Vapor phase has larger velocity than liquid and shaves the two-phase interface. Larger vapor mass flux intensifies the shear forces and dissipates the momentum intensively. In Fig. 13, the averaged uncertainty of frictional pressure drop is ±15.0%. As shown in Table 2, the differential pressure sensor has high accuracy. But the pressure drop fluctuates due to the operation of the working fluid pump. An extra uncertainty of ±10.0% is included. In order to ensure the accuracy, frictional pressure drop values lower than 3.5 $kPam^{-1}$ are excluded.

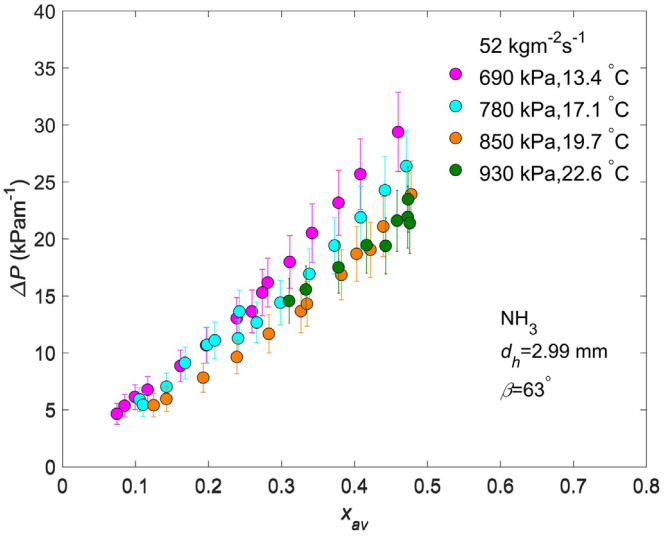

Fig. 14. Frictional pressure drop with varying averaged vapor quality at different condensation pressure.

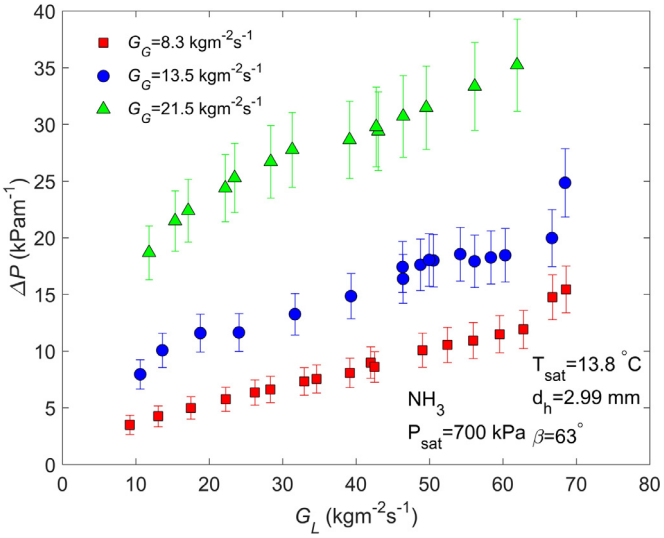

Fig. 15. Frictional pressure drop with varying liquid and vapor mass fluxes.

Fig. 14 shows the sensitivity to saturated pressures. The influence is negligible at low vapor qualities, and becomes noticeable at high vapor qualities. It is attributed to the change of vapor density. Higher saturated pressure has insignificant effects on liquid density, but increases vapor density remarkably. At high vapor qualities, higher saturated pressure decreases the averaged velocity because of the larger vapor density, and consequently reduces the momentum dissipation. Frictional pressure drop has an averaged uncertainty of ±14.2%.

Fig. 15 shows the influence of liquid and vapor mass fluxes separately, and both phases contribute to the frictional pressure drop. At different vapor mass fluxes, the frictional pressure drop increases with liquid mass fluxes, and the trend is similar. When the vapor mass flux increases from 13.5 to 21.5 $kgm^{-2}s^{-1}$, the frictional pressure drop more than doubles. In the same range of liquid mass flux, the frictional pressure drop increases about 1.2 times. This is in agreement with the phenomenon of separated flow. The vapor flow dominates the frictional pressure drop since the large velocity intensifies the momentum dissipation. During partial film flow, the trend lines with the variation of liquid mass fluxes are slightly steeper than during full film flow. The frictional pressure drop is less affected by the transition from full film flow to partial film flow, while the transition has significant influences on heat transfer.

6. Conclusions

This paper experimentally investigates NH_3 condensation in PHEs, and the conclusions are summarized below.

- In the tested ranges, the flow patterns are full film flow and partial film flow. The transition mainly depends on the wetting characteristics. Full film flow occurs at large liquid mass flux, while partial film flow takes place at small liquid mass flux. The inlet distribution also plays a role. The liquid is unevenly distributed among grooves close to the inlet, and becomes uniform along the flow direction.
- HTCs increase significantly with vapor qualities. HTCs decrease with mass fluxes from 21 to 42 $kgm^{-2}s^{-1}$, and then increase with mass fluxes in 42~78 $kgm^{-2}s^{-1}$. The transition is at the overall mass flux of 42 $kgm^{-2}s^{-1}$. HTCs decrease slightly with increased saturated pressures. Heat transfer is enhanced during partial film flow since vapor condenses directly on the dry zones.
- Frictional pressure drop increases sharply with vapor qualities and mass fluxes. Larger two-phase mass fluxes enhance the shear forces at the interface and at the wall. Frictional pressure drop slightly decreases with increasing saturated pressures.

The HTCs and frictional pressure drop show the characteristics of separated flow. The flow patterns result from the fluid properties of NH_3 and form the basis for the development of predicting models for NH_3 condensation in PHEs.

Declaration of Competing Interest

The authors declare that they have no known competing financial interests or personal relationships that could have appeared to influence the work reported in this paper.

CRediT authorship contribution statement

Xuan Tao: Conceptualization, Methodology, Formal analysis, Investigation, Data curation, Writing - original draft. **Elias Dahlgren:** Visualization, Data curation, Writing - review & editing. **Maaike Leichsenring:** Visualization, Data curation, Formal analysis, Writing - review & editing. **Carlos A. Infante Ferreira:** Conceptualization, Resources, Project administration, Funding acquisition, Writing - review & editing, Supervision.

Acknowledgments

This project has been developed in cooperation with Allseas Engineering B.V. The authors acknowledge the financial support from the China Scholarship Council and from the Koude Groep Delft / Wageningen. The authors are grateful to Edwin Overmars for providing the high speed camera. The transparent plate was manufactured in the EWI DEMO of TU Delft.

Supplementary materials

Supplementary material associated with this article can be found, in the online version, at doi:10.1016/j.ijheatmasstransfer.2020.119374.

References

[1] H. Mergner, K. Schaber, Performance analysis of an evaporation process of plate heat exchangers installed in a Kalina power plant, Energy 145 (2018) 105–115.
[2] H. Öhman, Implementation and evaluation of a low temperature waste heat recovery power cycle using NH_3 in an organic Rankine cycle, Energy 48 (2012) 227–232.
[3] Q. Shi, J. Zhu, M. Hertogh, Z. Sheng, Incentive mechanism of prefabrication in mega projects with reputational concerns, Sustainability 10 (2018) 1260.
[4] J. Chen, K. Zhu, X. Luo, Y. Chen, Z. Yang, Application of liquid-separation condensation to plate heat exchanger: comparative studies, Appl. Therm. Eng. 157 (2019) 113739.
[5] G.A. Longo, G. Righetti, C. Zilio, A new computational procedure for refrigerant condensation inside herringbone-type brazed plate heat exchanger, Int. J. Heat Mass Transf. 82 (2015) 530–536.
[6] H.B. Luan, J.P. Kuang, Z. Cao, Z. Wu, W.Q. Tao, B. Sundén, CFD analysis of two types of welded plate heat exchangers, Numer. Heat Transfer, Part A 71 (2017) 250–269.
[7] M. Wang, L. He, C.A. Infante Ferreira, Ammonia absorption in ionic liquid-s-based mixtures in plate heat exchangers studied by a semi-empirical heat and mass transfer framework, Int. J. Heat Mass Transf. 134 (2019) 1302–1317.
[8] X. Tao, C.A. Infante Ferreira, Heat transfer and frictional pressure drop during condensation in plate heat exchangers: assessment of correlations and a new method, Int. J. Heat Mass Transf. 135 (2019) 996–1012.
[9] L. Chen, Y.S. Tian, T.G. Karayiannis, The effect of tube diameter on vertical two-phase flow regimes in small tubes, Int. J. Heat Mass Transf. 49 (2006) 4220–4230.
[10] X. Tao, J.A. Kirkenier, C.A. Infante Ferreira, Condensation of NH_3 within a plate heat exchanger of small diameter channel, in: Proceedings of the 6th ASME International Conference on Micro/Nanoscale Heat and Mass Transfer, Dalian, China, 2019 paper 3920.
[11] X. Tao, M.P. Nuijten, C.A. Infante Ferreira, Two-phase vertical downward flow in plate heat exchangers: flow patterns and condensation mechanisms, Int. J. Refrig. 85 (2018) 489–510.
[12] S. Buscher, Visualization and modelling of flow pattern transitions in a cross–corrugated plate heat exchanger channel with uniform two-phase distribution, Int. J. Heat Mass Transf. 144 (2019) 118643.
[13] C. Jiang, B. Bai, Flow patterns and pressure drop of downward two-phase flow in a capsule-type plate heat exchanger, Exp. Therm. Fluid Sci. 103 (2019) 347–354.
[14] B.M. Fronk, S. Garimella, Condensation of ammonia and high-temperature-glide ammonia/water zeotropic mixtures in minichannels–Part I: measurements, Int. J. Heat Mass Transf. 101 (2016) 1343–1356.
[15] C.Y. Park, P. Hrjnak, NH_3 in-tube condensation heat transfer and pressure drop in a smooth tube, Int. J. Refrigeration. 31 (2008) 643–651.
[16] B.M. Fronk, S. Garimella, Condensation of ammonia and high-temperature-glide ammonia/water zeotropic mixtures in minichannels–Part II: heat transfer models, Int. J. Heat Mass Transf. 101 (2016) 1357–1373.
[17] X. Tao, E. Dahlgren, C.A. Infante Ferreira, Local NH_3 condensation in a plate heat exchanger, in: Proceedings of the 13th IIR Gustav Lorentzen Conference On Natural Refrigerants, Valencia, Spain, 2018 paper 1160.
[18] H.J. Kim, L. Liebenberg, A.M. Jacobi, Flow visualization of R-245fa boiling in a brazed plate heat exchanger (BPHE) near the micro-macroscale transition, in: Proceedings of the International Refrigeration and Air Conditioning Conference, Purdue, America, 2018.
[19] M. Nakamura, Y. Kawabata, T. Yasunaga, Y. Ikegami, The visualization of phase change phenomena in herringbone type plate heat exchanger using 3D-printer, in: Proceedings of the 27th International Symposium on Transport Phenomena, Honolulu, America, 2016.
[20] D. Lee, D. Kim, S. Yun, Y. Kim, Two-phase flow patterns and pressure drop of a low GWP refrigerant R-1234ze (E) in a plate heat exchanger under adiabatic conditions, Int. J. Heat Mass Transf. 145 (2019) 118816.
[21] da Silva Lima, R. J., J.M. Quibén, C. Kuhn, T. Boyman, J.R. Thome, Ammonia two-phase flow in a horizontal smooth tube: flow pattern observations, diabatic and adiabatic frictional pressure drops and assessment of prediction methods, Int. J. Heat Mass Transf. 52 (2009) 2273–2288.
[22] H. Arima, J.H. Kim, A. Okamoto, Y. Ikegami, Local boiling heat transfer characteristics of ammonia in a vertical plate evaporator, Int. J. Refrig. 33 (2010) 359–370.
[23] M. Leichsenring, Flow visualization of downward condensing ammonia in a gasketed plate heat exchanger Master thesis, Delft University of Technology, 2019.
[24] M. Leichsenring, X. Tao, C.A. Infante Ferreira, J.A. Kirkenier, Flow visualization of ammonia inside a gasketed plate heat exchanger condenser, in: Proceedings of the 25th IIR International Congress of Refrigeration, Montreal, Canada, 2019 paper 746.
[25] Lemmon, E.W., Huber, M.L., McLinden, M.O., 2013. NIST standard reference database 23: reference fluid thermodynamic and transport properties-refprop, version 9.1, national institute of standards and technology, standard reference data program, gaithersburg.
[26] X. Tao, E. Dahlgren, C.A. Infante Ferreira, Condensation heat transfer and pressure drop of NH_3 and NH_3/H_2O within a plate heat exchanger, in: Proceedings of the 25th IIR International Congress of Refrigeration, Montreal, Canada, 2019 paper 727.
[27] J.G. Collier, J.R. Thome, Convective Boiling and Condensation, Clarendon Press, Oxford, 1994.
[28] T.A. Jankowski, E.N. Schmierer, F.C. Prenger, S.P. Ashworth, A series pressure drop representation for flow through orifice tubes, J. Fluids Eng. 130 (2008) 051204.
[29] V. Grabenstein, S. Kabelac, Experimental and theoretical analysis of the local condensation heat transfer in a plate heat exchanger, J. Phys. Conf. Ser. 395 (2012) 012169.
[30] V. Grabenstein, A.-.E. Polzin, S. Kabelac, Experimental investigation of the flow pattern, pressure drop and void fraction of two-phase flow in the corrugated gap of a plate heat exchanger, Int. J. Multiph. Flow. 91 (2017) 155–169.
[31] K. Nilpueng, S. Wongwises, Two-phase gas-liquid flow characteristics inside a plate heat exchanger, Exp. Therm. Fluid Sci. 34 (2010) 1217–1229.
[32] C. Tribbe, H.M. Müller-Steinhagen, Gas/Liquid flow in plate-and-frame heat exchangers - Part II: two-Phase multiplier and flow pattern analysis, Heat Transf. Eng. 22 (2001) 12–21.
[33] P. Vlasogiannis, G. Karagiannis, P. Argyropoulos, V. Bontozoglou, Air water two-phase flow and heat transfer in a plate heat exchanger, Int. J. Multiph. Flow. 28 (2002) 757–772.
[34] D. Winkelmann, Condensation of pure refrigerants and their zeotropic mixtures in plate heat exchangers Ph.D. thesis, Commissiariat à l'energie atomique (CEA), 2010.
[35] A.M. Barajas, R.L. Panton, The effects of contact angle on two-phase flow in capillary tubes, Int. J. Multiph. Flow. 19 (1993) 337–346.
[36] C. Zhang, C. Shen, Y. Chen, Experimental study on flow condensation of mixture in a hydrophobic microchannel, Int. J. Heat Mass Transf. 104 (2017) 1135–1144.
[37] L. Galbiati, P. Andreini, The transition between stratified and annular regimes for horizontal two-phase flow in small diameter tubes, Int. Commu. Heat Mass. 19 (1992) 185–190.
[38] J. Wang, W. Gao, H. Zhang, M. Zou, Y. Chen, Y. Zhao, Programmable wettability on photocontrolled graphene film, Sci. Adv. 4 (2018) eaat7392.
[39] K. Sarraf, S. Launay, L. Tadrist, Complex 3D-flow analysis and corrugation angle effect in plate heat exchangers, Int. J. Therm Sci. 94 (2015) 126–138.
[40] P. Hrnjak, C. Kondou, Refrigerant side heat transfer in condensers with round tubes, in: Proceedings of the 4th IIR Conference on Thermophysical Properties and Transfer Processes of Refrigerants, Delft, The Netherlands, 2013 paper TP-087.
[41] C. Kondou, P. Hrnjak, Condensation from superheated vapor flow of R744 and R410A at subcritical pressures in a horizontal smooth tube, Int. J. Heat Mass Transf. 55 (2012) 2779–2791.
[42] H. Martin, Pressure drop and heat transfer in plate heat exchangers, in: P. Stephan, H. Martin, S. Kabelac, D. Mewes, M. Kind, K. Schaber (Eds.), VDI Heat Atlas, 2nd Ed., Springer, Dusseldorf, 2010, pp. 1516–1521.
[43] M.S. El-Genk, H.H. Saber, Minimum thickness of a flowing down liquid film on a vertical surface, Int. J. Heat Mass Transf. 44 (2001) 2809–2825.
[44] D.E. Hartley, W. Murgatroyd, Criteria for the break-up of thin liquid layers flowing isothermally over solid surfaces, Int. J. Heat Mass Transf. 7 (1964) 1003–1015.
[45] W.S. Kuo, Y.M. Lie, Y.Y. Hsieh, T.F. Lin, Condensation heat transfer and pressure drop of refrigerant R-410A flow in a vertical plate heat exchanger, Int. J. Heat Mass Transf. 48 (2005) 5205–5220.